RAA 2019 Vol. 19 No. 11, 160(14pp) doi: 10.1088/1674–4527/19/11/160

http://www.raa-journal.org http://iopscience.iop.org/raa

Research in Astronomy and Astrophysics

Hard X-ray Imager (HXI) onboard the ASO-S mission

Zhe Zhang[1], Deng-Yi Chen[1], Jian Wu[1], Jin Chang[1], Yi-Ming Hu[1], Yang Su[1,2], Yan Zhang[1], Jian-Ping Wang[3], Yao-Ming Liang[4], Tao Ma[1], Jian-Hua Guo[1], Ming-Sheng Cai[1], Yong-Qiang Zhang[1], Yong-Yi Huang[1], Xiao-Yan Peng[1], Zong-Bin Tang[3], Xuan Zhao[3], Hong-He Zhou[3], Lian-Guo Wang[4], Jing-Xing Song[4], Miao Ma[4], Guang-Zhou Xu[5], Jian-Feng Yang[5], Di Lu[5], Ying-Hong He[5], Jin-You Tao[5], Xiao-Long Ma[5], Bao-Gang Lv[5], Yan-Ping Bai[3], Cai-Xia Cao[3], Yu Huang[1] and Wei-Qun Gan[1]

[1] Key Laboratory of Dark Matter and Space Astronomy, Purple Mountain Observatory, Chinese Academy of Sciences, Nanjing 210034, China; *zhangzhe@pmo.ac.cn*

[2] School of Astronomy and Space Science, University of Science and Technology of China, Hefei 230026, China

[3] Innovation Academy for Microsatellites, Chinese Academy of Sciences, Shanghai 201203, China

[4] National Space Science Center, Chinese Academy of Sciences, Beijing 100190, China

[5] Xi'an Institute of Optics and Precision Mechanics, Chinese Academy of Sciences, Xi'an 710119, China

Received 2019 August 12; accepted 2019 September 16

Abstract Hard X-ray Imager (HXI) is one of the three scientific instruments onboard the Advanced Space-based Solar Observatory (ASO-S) mission, which is proposed for the 25th solar maximum by the Chinese solar community. HXI is designed to investigate the non-thermal high-energy electrons accelerated in solar flares by providing images of solar flaring regions in the energy range from 30 keV to 200 keV. The imaging principle of HXI is based on spatially modulated Fourier synthesis and utilizes about 91 sets of bi-grid sub-collimators and corresponding $LaBr_3$ detectors to obtain Fourier components with a spatial resolution of about 3 arcsec and a time resolution better than 0.5 s. An engineering prototype has been developed and tested to verify the feasibility of design. In this paper, we present background, instrument design and the development and test status of the prototype.

Key words: instrumentation: detectors — space vehicles: instruments — Sun: X-ray — techniques: imaging spectroscopy

1 INTRODUCTION

The Advanced Space-based Solar Observatory (ASO-S) satellite is China's first space science mission for solar physics (Gan et al. 2019). It is proposed for the solar maximum (around 2022∼2025) of the 25th solar cycle, and is expected to be launched in 2022. The scientific objectives of ASO-S, summarized as "1M2B," focus on the simultaneous observations of solar magnetic field, solar flares, coronal mass ejections (CMEs) and the relationships between them. Three scientific payloads, the Lyman-alpha Solar Telescope (LST) for CME observations, Full-disk vector MagnetoGraph (FMG) for the solar magnetic field and Hard X-ray Imager (HXI) which aims to observe X-ray bursts from flares, are designed for these objectives and installed on a single platform.

As one of the most violent energy bursts in the solar system, solar flares have always been a research focus in solar physics and a vital clue for studies of the energy release mechanisms in solar activities (see the reviews of flares in Priest & Forbes 2002; Fletcher et al. 2011; Benz 2017), which involve magnetic reconnection, plasma heating, particle acceleration and enhanced emission across the whole electromagnetic spectrum from radio, infrared to X-ray and gamma ray. Magnetic reconnection is a fundamental process of energy release and conversion in the cosmic plasma system, and the core process in flares. As direct products of reconnection, heated plasma (from a few to tens of MK) and accelerated particles provide an important diagnostic through their bremsstrahlung emission in X-rays and gamma rays.

HXI targets hard X-rays emitted from energetic electrons in solar flares, which is a key link in flare research. In the standard picture of flares, electrons are accelerated by reconnection in the corona, transported along newly-formed magnetic loops down to the lower atmosphere, causing a series of processes, such as impulsive heating, evaporation, brightened ribbons, etc. Therefore, energetic electrons are essential not only for studies of reconnection, but also for flare kinetics. However, many details of these processes remain unknown, such as the location and mode of particle acceleration, the relationship with magnetic field topology, and the propagation and escape of high-energy particles.

Fourier-transform imaging has been demonstrated as a kind of efficient technique for high energy solar imaging in recent decades. HXI employs an imaging technique by spatial modulation similar to that by the Hard X-ray Telescope (HXT) onboard the Japanese Yohkoh mission (1991∼2001) (Kosugi et al. 1991), and to that used by the Reuven Ramaty High Energy Solar Spectroscopic Imager (RHESSI) mission (2002∼2018) (Lin et al. 2002) and the Spectrometer/Telescope for Imaging X-rays (STIX) (Krucker et al. 2016) onboard the Solar Orbiter mission (to be launched in 2020).

Through continuous imaging, spectral and temporal detection, HXI can obtain rich characteristic information on flares at the same time, such as location, shape, radiation intensity and time evolution (more details on the scientific observation of HXI can be found in Su et al. 2019 of this special issue.). It is of great scientific significance to study the acceleration mechanism, to determine the location and scope of the source area of the acceleration region, to study particle transport mechanism and to compare the processes in different flares. Specifically:

(1) It will provide analysis capabilities of hard X-ray imaging, spectroscopy and imaging spectroscopy, as a diagnostic tool for non-thermal processes observed by both HXI and LST;
(2) It will provide high energy imaging data of the Sun from perspective of the Earth during the 25th solar maximum;
(3) It will, together with Solar Orbiter/STIX, supply for the first time multi-angle stereoscopic observations of solar flares in X-rays, which is of great significance for diagnosing anisotropic high-energy processes (Krucker et al. 2019);
(4) It will facilitate cooperation with LST and FMG to provide comprehensive information on solar eruption activities, and make breakthroughs in understanding the triggering of solar eruptions, the correlation between flares and CMEs and other important scientific issues;
(5) It can also enable the prediction of flare-related solar energetic particles (SEP), to help prevent or reduce the impacts of potentially disastrous space weather on satellites, human space activities and even power grids on the ground.

In this paper, we will outline the imaging principle and overall design of HXI in Section 2. Then the detailed design of each part of the instrument and the development progresses will be presented in Section 3. A summary and outlook will be given in the last section.

2 OVERVIEW OF HXI DESIGN

The imaging capability of HXI is based on the so-called spatially modulating Fourier-transformation technique. The principle of this imaging technique has been described in detail by Su et al. (2019). In brief, the intensity of incoming X-rays from solar flares is modulated in the form of a triangular wave function according to the incident direction. Its period is related to the pitch of the bi-grid subcollimator (Fig. 2). As a result, different two-dimensional Fourier components, or visibilities, are approximately obtained by choosing different pitches and position angles of subcollimators. The intensity of flux modulation is measured and recorded by the detector behind each subcollimator, which is related to visibility and used for offline image reconstruction. The configuration of pitch and position angle of subcollimators should be carefully chosen to balance the requirements of spatial resolution and imaging range for different scales and positions of HXR sources as much as possible. In addition to the careful consideration for the range (corresponding to the maximum and minimum pitches), we also considered that the coverage of the uv plane should be as even as possible.

HXI implements 91 spatially modulating subcollimators which consist of nearly 1200 mm separated grid pairs and 91 $LaBr_3$ detectors behind each subcollimator, to modulate and detect incident X-rays. The other eight identical $LaBr_3$ detectors are utilized to measure the total flux and charged particle background. Forty-five visibilities are measured by 44 pairs of cos-sin subcollimators and one single set of three subcollimators. For cos-sin subcollimators, 10 groups of grids with pitches from 36 μm to 1224 μm and 3∼5 kinds of position angles for each pitch are employed (Table 1). In other words, HXI obtains spatial resolution from 3 arcsec to more than 100 arcsec, which covers most HXR sources (Dennis & Pernak 2009; Warmuth & Mann 2013). The set with three subcollimators has the same pitch (1224 μm) and position angle, and there is a 120° phase difference between them. Since not only visibility information but also total flux value can be determined from the data of this set, it is applicable as a special backup for the total flux monitor of HXI.

The overview of HXI is depicted in Figure 2. It consists of three major parts from the viewpoint of structure, the Collimator (HXI-C), Spectrometer (HXI-S), and Electronic Control Box (HXI-E), which can be simply compared to the lens, CCD and controller of a camera,

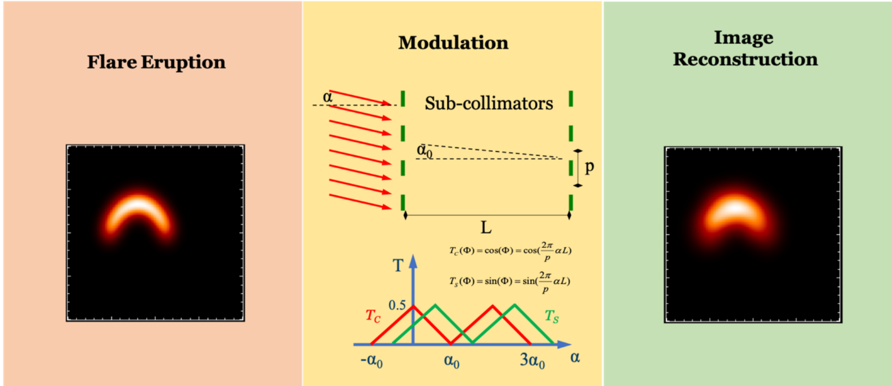

Fig. 1 Imaging principle applied by HXI. *Left*: A flare loop is generated on the solar surface; *Middle*: Hard X-ray flux from the flare arrives at Earth orbit and is modulated by a collimator (sub-collimator arrays with different pitches and position angles) with its direction. Photons passing through the collimator are recorded by detectors; *Right*: Modulated data are used to reconstruct the flare image on the ground.

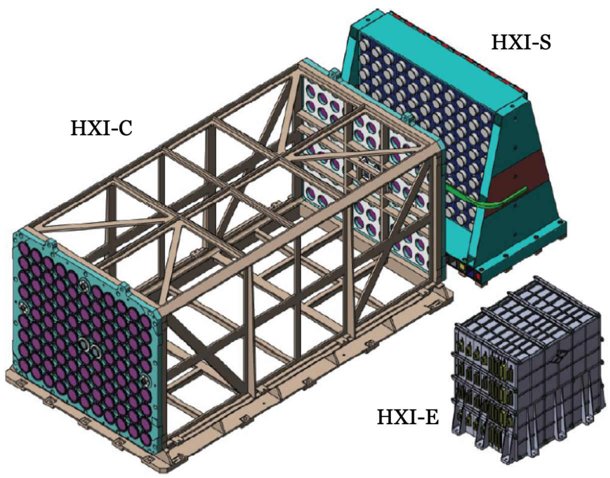

Fig. 2 Schematic drawing of HXI.

Table 1 Collimator Grid Configuration of HXI

	Pitch /μm	36	52	76	108	156	224	344	524	800	1224	Total Quantity /pair
	Slit /μm	20	31	46	54	78	112	172	262	400	612	
	Nominal spatial resolution (FWHM) / $''^{(1)}$	3.1	4.5	6.5	9.3	13.4	19.3	29.6	45.1	68.8	105.2	
	Thickness / mm	1.0	1.4	1.7	2.0	2.0	2.0	2.0	2.0	2.0	2.0	
Quantity	Total	8	10	10	10	10	10	10	10	6	7	91
	$\triangle\Phi^{(2)} = 0°$ (cosine type)	4	5	5	5	5	5	5	5	3	3	45
	$\triangle\Phi = 90°$ (sine type)	4	5	5	5	5	5	5	5	3	2	44
	$\triangle\Phi = 120°$	0	0	0	0	0	0	0	0	0	1	1
	$\triangle\Phi = 240°$	0	0	0	0	0	0	0	0	0	1	1
	Position angle / °	Ongoing optimization										
	Effective dimension (slit & slot)	ϕ36mm circle for all front grids, and ϕ22mm for rear grids										
	Material	0.1 mm thick tungsten foil										
	Distance between the front and rear grids	$L = 1190$ mm										

(1) The definition of spatial resolution is generally expressed as FWHM = $p/2L$; (2) $\triangle\Phi$ is the phase difference between the front and rear grids of a subcollimator. In the cosine type case, slits of the front grid just line up with the corresponding slits of the rear grid, and $\triangle\Phi$ is zero.

respectively. While HXI-C and HXI-S are mounted upside down on the optical reference plate outside the spacecraft with two other instruments to meet the requirement of simultaneous observation, HXI-E is mounted inside the spacecraft to obtain a better working environment. The three parts are only connected to each other by cables.

The main structure of HXI-C is a titanium alloy framework with two plates at each end. The front and rear plates are 1190 mm apart (Fig. 3). Ninety-nine mounting posi-

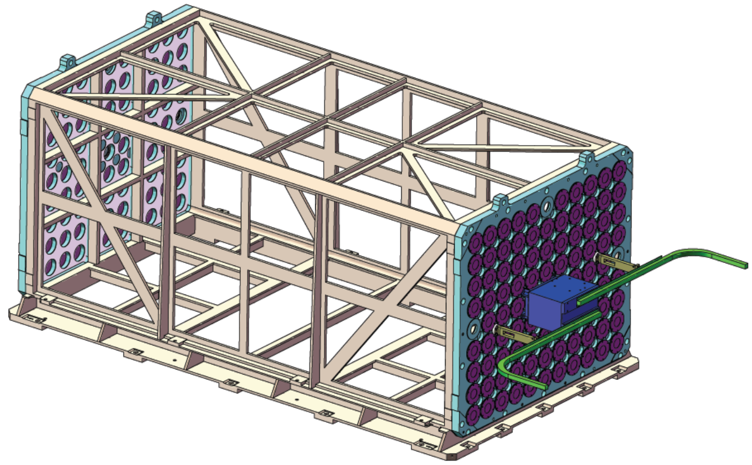

Fig. 3 HXI-C, including grids (*purple*), front and rear base plates (*cyan*), titanium alloy framework (*grey*) and solar aspect system (SAS, *blue*). To enhance the rigidity and intensity of the total system, some ribs are designed either on the top or on the side. Two heat pipes (*green*) serve as the thermal control for electronics incorporated in SAS.

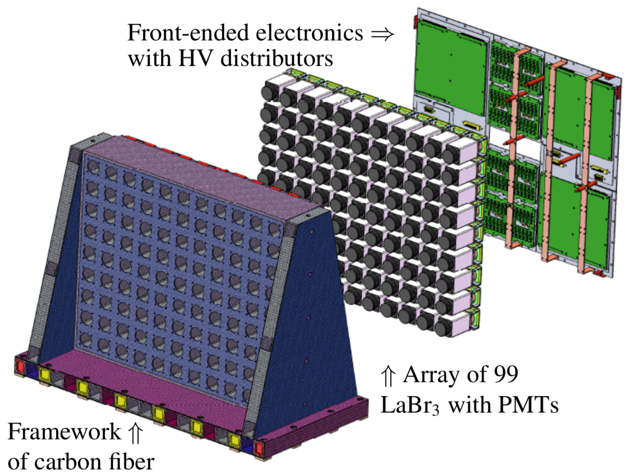

Fig. 4 Exploded view of HXI-S. Ninety-nine sets of $LaBr_3$ detectors mounted in the CFRP framework to form a 9×11 array. FEEs and high voltage distributors are fixed on the shielding plate. Heat generated by working PMT base boards will be transferred to the shielding plate with the help of copper strips, which can be seen above the FEE boards.

tions, each with an interval of 50 mm, are arranged in an array of 9×11 on both plates. Ninety-one of them are occupied by tungsten grid pairs to modulate the incident X-rays. An SAS including two CMOS cameras is also installed on the framework, consuming five installation positions. A single lens on the front plate and a CMOS detector placed on the rear plate toward the lens constitute one camera to provide axis direction information of X-ray imaging with respect to the solar disk by measuring the white-light image of the Sun. Three pieces of frosted glass on the front plate and another CMOS camera mounted on the rear plate are used to monitor the relative distortion of framework by measuring the image of the frosted glass. In addition, the open grids installed in the remaining three locations are utilized for total flux detection.

HXI-S has a CFRP framework, in which 99 detectors are composed of $LaBr_3$ scintillators and photomultiplier tubes (PMTs), and front-end electronics (FEEs) and high voltage distributors are mounted. X-ray counting, accomplished by modulation of one or total flux through subcollimators, is detected by the corresponding detectors. Then the signals from all detectors are processed and recorded as the energy spectrum formed simultaneously by FEEs. The time resolution or spectral um acquisition time can be automatically adjusted according to the total X-ray flux from the Sun between 0.125 s and 4 s.

HXI-E is in charge of mission operation, data processing and power supply of HXI. It has a sandwich-like structure where a data processing unit, a data management unit, four high voltage power supply boards and two DC-DC

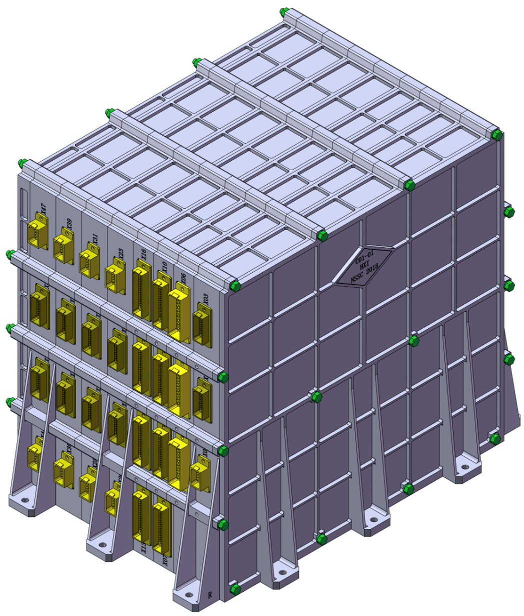

Fig. 5 Schematic diagram of HXI-E.

power supply boards are inserted one by one and fixed (Fig. 5). All scientific data from HXI-S and HXI-C will be packaged by HXI-E together with time information and sent to a mass storage device on the satellite platform. Finally, these data will be transmitted to the ground together with other housekeeping data for image reconstruction and analysis.

The main characteristics of HXI are listed in Table 2.

Table 2 Main Characteristics of HXI

Energy range	$30 \sim 200$ keV
Energy resolution (FWHM)	$\leq 27\%$ @32 keV
Spatial resolution	$\leq$ **3.5″**@30 keV
Field of View	$\geq 40'$
Time resolution (statistically limited)	≤ 0.5 s

3 INSTRUMENT

An engineering prototype of HXI has been developed to verify the design and some key technologies in the past Phase-B study. The detailed design of HXI and developing progress of the prototype will be described here.

3.1 HXI-C

HXI-C is the key part of HXI and its performance will affect the quality of imaging directly. It can be simply divided as X-ray optics and visible-light optics. X-ray optics include grids and titanium alloy framework. On the other hand, visible-light optics just refer to the SAS. For the X-ray optics, most of the development work is focused on how to improve and maintain accuracy of the grid assembly for the subcollimator, for example, the grid fabrication, framework stability, high precision assembly and thermal control.

3.1.1 Grids

The grid is the basic component of the collimator. Several key points should be considered and paid attention to during design and production.

The first is the effective area of the grid. It is related to the field of view that needs to be large enough to cover the entire solar disk ($\sim$32 arcmin). As shown in Table 1, the diameter of **the slit array** is set as 34 mm for the front grid and 22 mm for the rear grid. The difference between these two diameters and the spacing between the front and rear grids together determines the field of view of each subcollimator, more than 40 arcmin.

The second is the thickness of the grid. In order to achieve an ideal X-ray modulation effect, the grid should be as thin as possible, while still effectively blocking X-rays at a given energy. This means that the grid material must be a metal with high atomic number Z. Considering the mechanical properties of the material and the results of comparison of grid trial production, tungsten is chosen as the grid material of HXI. The thickness of grids with different pitches is also determined to be 1 mm $\sim$2 mm by carefully calculating and trading off the modulation efficiency at different energy ranges (Su et al. 2019).

Thirdly, an appropriate fabricating technique needs to be chosen. Through a series of trial productions and improvement techniques, an ultrashort pulse laser cutting technique is employed to produce grids with acceptable cost and reasonable efficiency. The manufacturing task of the grid is undertaken by two Chinese laser machining companies, Xi'an Micromach Technology, who produced the grids including 36 μm pitch type, and Suzhou Delphi Laser. The grid productions are carefully checked and measured. The pitch error and cumulative error in a series of slits are both less than 1 μm.

Finally, how should we accurately stack grids? Unlike the etching technique that limits the thickness of materials which should be near the width of the grid slit, the current thickness of grids is 100 μm, even for 36 μm pitch under the technical limit of laser cutting. Therefore, only 10$\sim$20 layers of grids need to be stacked. A special high precision clamping is developed to assist the grid stacking process. The square holes on the grid are machined with grid slits at the same time, and the relative distance between the square holes and the grid slits is also kept at the same accuracy level of μm. When stacking, the special alignment pins on the clamping passing through the square holes of grids one by one will naturally guarantee that the stacking accuracy is better than 3 μm.

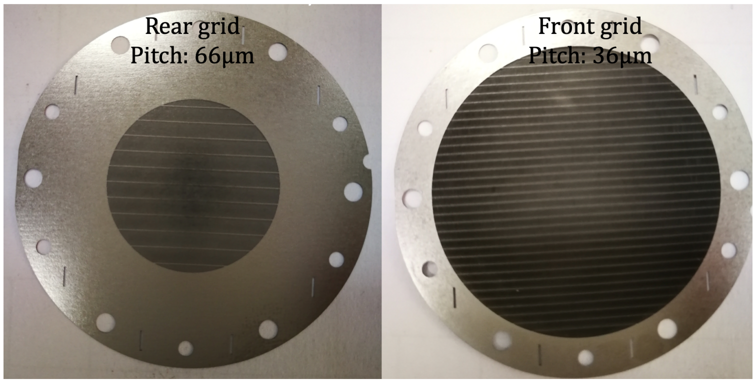

Fig. 6 Grids of HXI, produced by Xi'an Micromach Technology. The left is a rear grid with 66 μm pitch, and the diameter of the slit array is 22 mm; the right is a front grid with 36 μm pitch, and the diameter of the slit array is 36 mm.

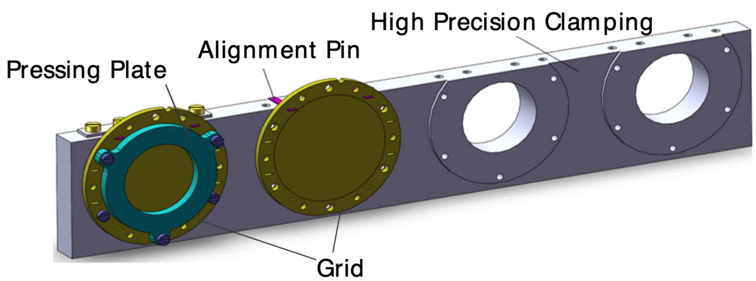

Fig. 7 High precision clamping used for grid stacking.

3.1.2 Assembly and alignment

In fact, there are always some errors and misalignments during the manufacture, assembly and testing of instruments. This means that the actual modulation will deviate from the ideal design. Knowledge of the errors and misalignments is very helpful to improve the quality of image reconstruction. Although a self-calibration method using observed data has been demonstrated to be effective with Yohkoh/HXT (Sato et al. 1999) and RHESSI to obtain this information and help to improve the quality of the reconstructed image, the alignment and structure stability requirements are still critically enumerated as several technical indexes for HXI-C according to the experiences from RHESSI and our specific technical conditions:

(1) The translation deviation of alignment between the front and rear grids should be less than 36 μm;
(2) The alignment deviation between any pair of sine and cosine subcollimators should be less than 3 μm;
(3) The twist of front or rear grid with respect to the other should be less than 10 arcsec;
(4) During launching and on-orbit operation, the instrument will experience some different environmental conditions, such as vibration and temperature changes, but the above-mentioned accuracy indicators should remain unchanged once the working condition recovers.

To control the misalignment, the assembly of HXI-C includes three steps:

(1) The front and rear plates are fixed together. The grids are mounted and aligned with the help of a coordinate image measuring machine, and the accuracy of the grid is better than 1.5 μm. Moreover, reference surfaces are formed on the side of both plates by simultaneous grinding (Fig. 8);
(2) Two plates are separated and mounted on the framework as displayed in Figure 9. High precision marble positioning tools are used for the alignment of plates while positioning surfaces formed in the last step are set as benchmarks. A coordinate measuring machine with accuracy better than 3 μm is also employed to measure the reference surfaces to ensure the alignment accuracy of plates after installation;
(3) Environmental qualification, including all kinds of vibrational and thermal tests, based on the satellite requirements and accuracy of alignment monitoring, are performed to demonstrate that the stability of HXI-C meets the requirements.

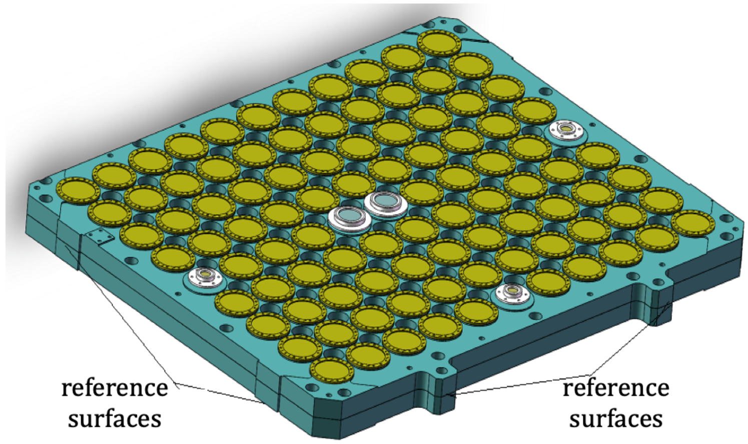

Fig. 8 Grid installation and alignment.

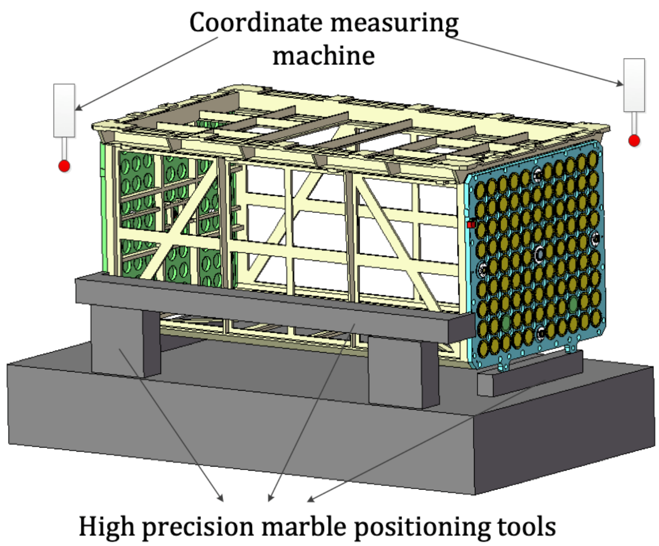

Fig. 9 Plate assembly and alignment.

So far, assembly of the HXI-C prototype has been completed (as seen in Fig. 10), and the alignment accuracy has been verified. However, the 3rd step is still in progress.

3.1.3 Thermal control of HXI-C

It is easy to understand that a good and stable thermal environment helps the HXI-C to maintain alignment accuracy. Therefore, an active thermal control system is employed to reduce the effect of temperature. The thermal environment of HXI is relatively friendly since the spacecraft is designed for triaxial stability and always focuses on the Sun. Good temperature control can be achieved by consuming relatively few resources.

First of all, HXI-C is covered with 15 layers of multilayer insulation material to isolate the heat exchange between outer space and the collimator itself. As seen in Figure 11, several heaters are pasted on the front and rear plates and the bottom of the titanium alloy framework. According to the simulation results, the temperature difference between front and rear plates can be kept below 1° C by using active thermal control under the power limit. The temperature gradient at the bottom of the framework is also controlled below 1° C. These results are also validated during the thermal experiment for structure and thermal control design verification.

3.1.4 Solar aspect system

As is well known, the stability of the optical path is important for imaging. Although the ASO-S spacecraft pointing accuracy can only be maintained at the arcminute-level ($\sim$36 arcsec), HXI needs to obtain arcsecond-level images. The SAS, which helps to obtain high-precision pointing information over longer observation periods by measuring the white light imaging of the Sun, is a common compo-

Fig. 10 Assembly and alignment of HXI-C prototype.

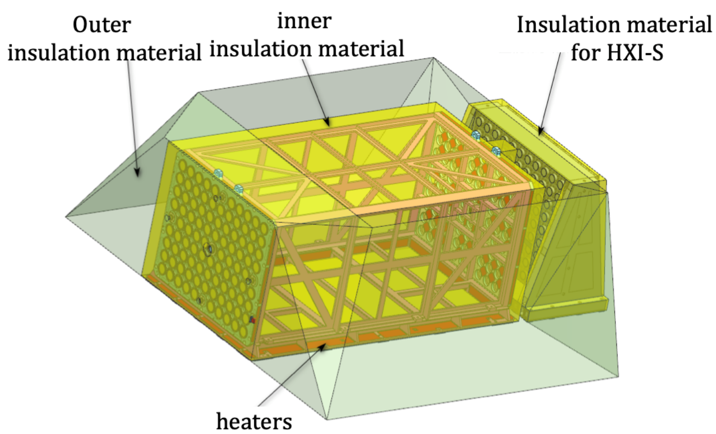

Fig. 11 Schematic diagram for active thermal control design.

nent in a solar high energy imaging instrument. In addition, it is also important in the joint analysis with data from other bands because X-ray optics cannot independently determine the location of X-ray sources imaged on the Sun's surface. In addition to the above functions, the SAS of HXI is also implemented to measure the relative displacement between the front and rear plates, both on the ground and in orbit.

According to the function requirements, the SAS of HXI consists of two parts, the Solar Aspect (SA) and the Displacement Monitor (DM). SA incorporates a lens on the front plate and a CMOS detector on the rear plate. The DM includes an incident window and three sets of frosted glass on the front plate, and a CMOS detector with lenses set on the rear plate. CMOS chips with $2\text{k}\times2\text{k}$ pixels and a pixel size of 5.5 μm are chosen for both SA and DM. Both chips are fixed with a set of front-end electronics and data processing circuits in an electronic control box mounted on the rear plate, which is diagrammed in Figure 12.

For SA, sunlight is focused by a lens on the front plate and imaged on a CMOS detector (Fig. 13). The solar image covers almost the entire CMOS region with a fixed focal length of nearly 1200 mm. Four square areas in the corner of the detector are chosen and the image of the Sun covering each area is recorded as an area value. These data, in the form of four quadrant data, will be transmitted directly to the ground without further processing to maintain simplicity and be used to calculate the central coordinates of the Sun or the pointing information. The data rate is fixed at 4 Hz as a tradeoff between X-ray imaging requirements and electronic capacity. The pointing accuracy is expected to be less than 1 arcsec according to the completed simulation test.

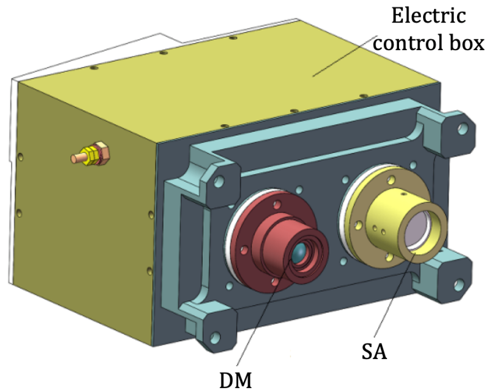

Fig. 12 Electric control box of SAS.

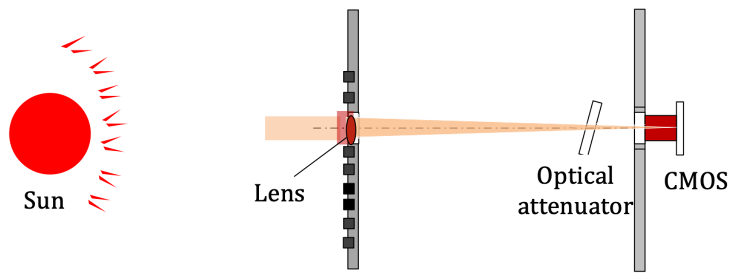

Fig. 13 The working principle of SA.

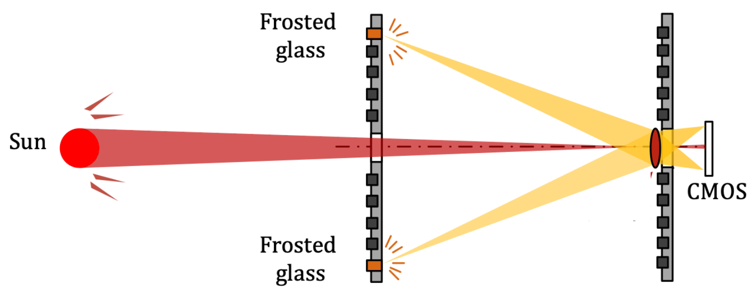

Fig. 14 The working principle of DM.

For DM, three sets of frosted glass will be simultaneously imaged on the detector when they are lighted by additional LEDs on the ground or sunlight on orbit. The displacements between the front and rear plates can be monitored by measuring and calculating the coordinates of the image. The coordinates will be calculated online and transmitted to the ground for further analysis. The translation and rotation measuring accuracy can be achieved better than 3 μm and 3 arcsec, respectively. In addition, the solar disk is also imaged by DM using light through the incident window. It can only be used as a backup of DM due to the low signal-to-noise ratio caused by the small size of the image.

By the way, more details about HXI-C can be found in another paper submitted to the SPIE conference (Chen et al. 2019).

3.2 HXI-S

HXI-S records the solar X-rays with both high energy resolution and time resolution for each subcollimator modulation. As illustrated in Figure 4, it is composed of 99 $LaBr_3$ scintillation detector modules, eight sets of FEEs and high voltage distribution boards.

3.2.1 Pile-up

Because of the large dynamic range of flare intensity, avoiding signal pile-up has always been considered as a

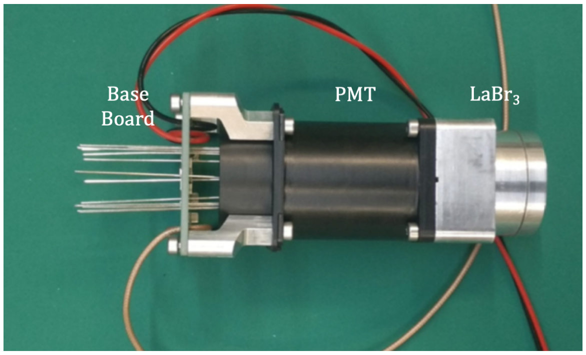

Fig. 15 Prototype of an $LaBr_3$ detector module.

major challenge for HXI and similar past solar high energy detectors. While RHESSI and STIX employ a movable attenuator, HXI chooses another way to solve this. It is known that the X-ray photon counts from flares decrease at a power-law rate with the increase of energy, and HXI only needs to detect X-rays higher than 30 keV. As a result, we can choose the appropriate detectors and FEEs which are fast enough to satisfy the detection demand for the vast majority of flare events.

3.2.2 *Detector modules*

A non-position-sensitive scintillation detector, including an $LaBr_3$ scintillator, a PMT and a base circuit, is used to "count" photons passing through the subcollimator with energy resolution during an exposure (Fig. 15).

$LaBr_3$ crystals produced by the Beijing Glass Research Institute (BGRI) have excellent performances, such as high light yield, a fast decay time and good energy resolution. Crystals with size of $\phi 25\,\text{mm} \times 25\,\text{mm}$ are packaged by an aluminum shield to avoid deliquescence. Considering the thickness of multilayer insulation material covering HXI, shield thickness at the front of the crystal is chosen to be 2 mm to avoid pulse pile-up. The photon flux below 20 keV will be attenuated, and photons above 30 keV will not lose too much (Zhang et al. 2019). The PMTs, R1924A-100-01, produced by Hamamatsu Photonics with super bi-alkali cathodes were selected to guarantee energy resolution of X-ray photons around 30 keV. A permalloy shield is utilized for each PMT to reduce the magnetic field and suppress gain variation. The base circuit, based on Hamamatsu socket E2924-05, is designed to maintain linearity and gain stability at high event rates. An LED test has demonstrated that it can provide good linearity and gain stability with event rate higher than 100 kHz (Zhang et al. 2019). In addition, Barium-133 is chosen as the calibration source on orbit for the detector of HXI-C. Its characteristic X-rays of 30 keV to 383 keV could be used to calibrate the gain degradation of PMTs and the dependence of FEEs on temperature. The intensity of the source is still being studied to trade off reducing the intrinsic background and acquiring time of calibration spectra. All the observation data without flares could be employed for calibration.

3.2.3 *Front-end electronics*

Eight sets of identical read out circuits receive charge pulses from 12 or 13 PMTs with a 16-channel charge measurement ASIC which accounts for the cost of FEEs in HXI-S. Under the control of a field-programmable gate array (FPGA), the analog output of ASIC will be digitalized and accumulated to a spectrum. HXI-E will send out synchronization pulses to synchronize all FEEs' start and stop times of spectrum accumulation.

Obviously, ASIC is the core component of FEE. IDE3381, from IDEAS, in Norway, is an improved version of its IDE3380 production with optimizations in dynamic range and readout speed just for the requirement of high counting rates in solar observations (Fig. 16).

In addition to spectral data applied for image reconstruction, FEEs also produce two other types of data simultaneously with the help of ASIC. First, event data, including trigger information, can be used for on-orbit trigger threshold calibration. Second, the counting data, which come from the trigger counters in the ASIC, can be operated for flux correction of spectrum and coarse indirect imaging that targets high intensity flares.

Only IDE3380 has been used and tested in the prototype by now because the design and production of IDE3381 has not been finished. IDE3381 production will be available in the qualification model of HXI.

3.3 HXI-E

HXI-E manages the whole observation mission in orbit, such as the reception and transmission of scientific data and housekeeping data from HXI-C and HXI-S, the power supplies for HXI-C and HXI-S, management and execution of instructions from the ground and so on. Because of the importance of its functions, redundant cold backup design is incorporated in HXI-E. This design greatly improves its reliability.

The functions like mission control and management of housekeeping data are relatively general, so only the scientific data processing and high voltage power supply will be introduced.

A data processing unit will send acquisition synchronization signals to eight FEEs in HXI-S and SAS in HXI-C at specified time intervals or after detecting eruption. Then the collected scientific data together with time and status information will be received and packaged into the data package. These data packages will be sent to the satellite

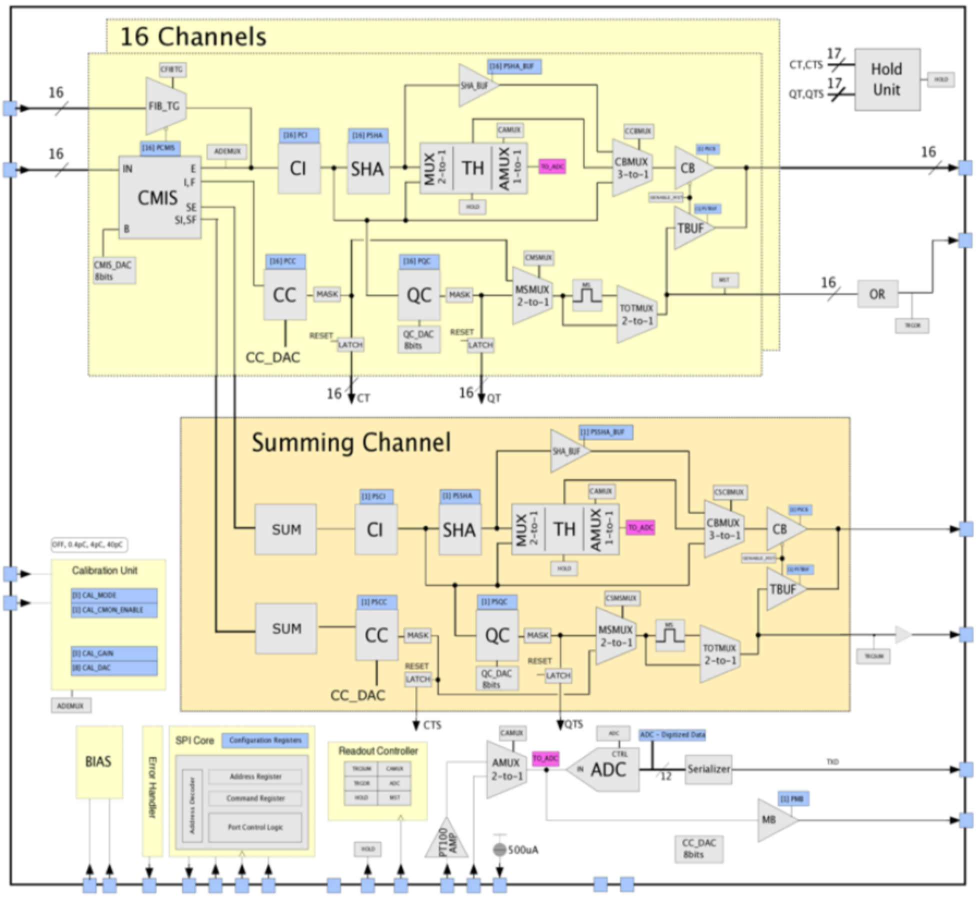

Fig. 16 Block diagram of charge measurement ASIC (adopted from Meier et al. 2016).

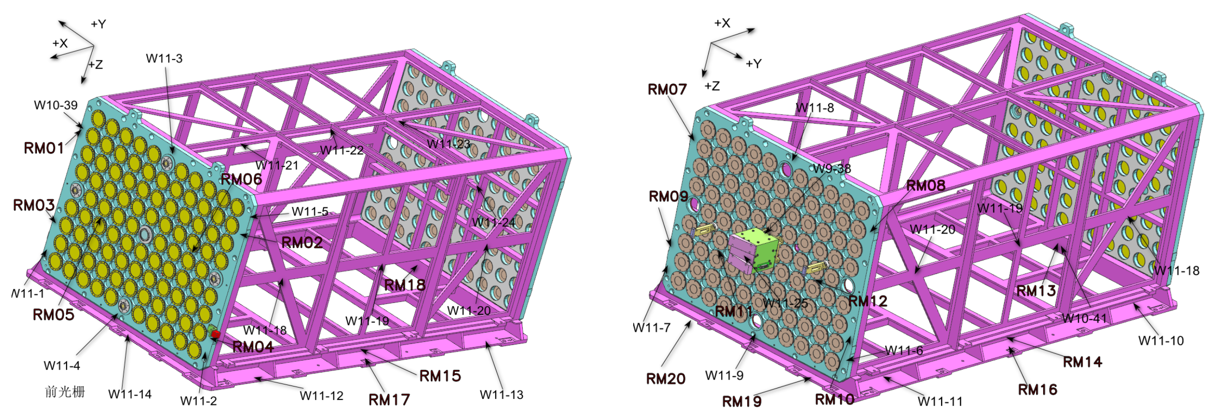

Fig. 17 Thermistor and thermocouple distribution of the prototype.

through the LVDS interface and transmitted to the ground together with the data from the other two ASO-S payloads. Furthermore, HXI-E needs to calculate flux from the Sun's direction, using the data from the total flux detector and background detector, to provide a reference eruption trigger signal to the other two payloads.

A high-voltage power supply board supplies nearly 1000 V of high voltage to several detector modules in HXI-S. S9032, a kind of high-voltage power supply module from SITEAL, in Italy, is employed with a 7 mA output current and 0∼1000 V output voltage. Four high-voltage power supply boards are mounted in HXI-E, each of which includes four units of the S9032 module and a set of high voltage control circuits. The data management unit will control the high voltage output through high voltage control circuits. Four units of S9032 on the high-voltage power

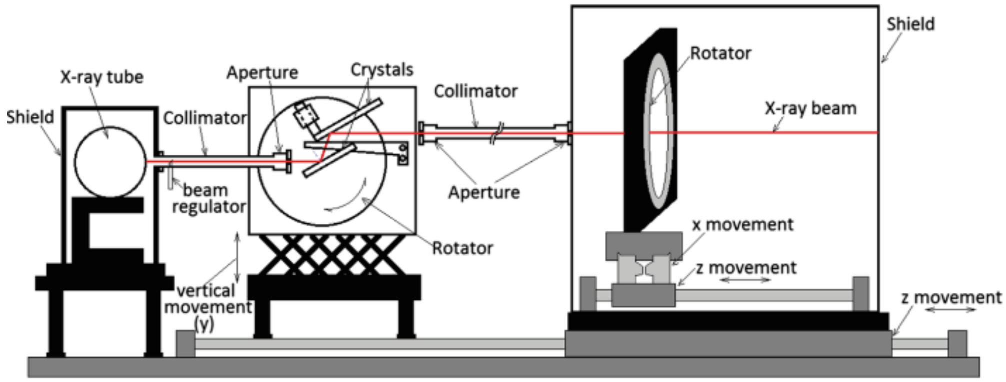

Fig. 18 The schematic diagram of the HXCF (adopted from Zhou et al. 2014).

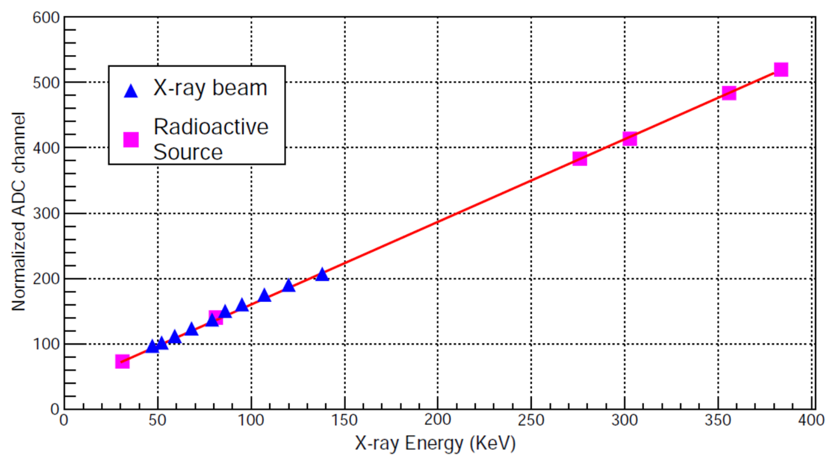

Fig. 19 Energy linearity test results.

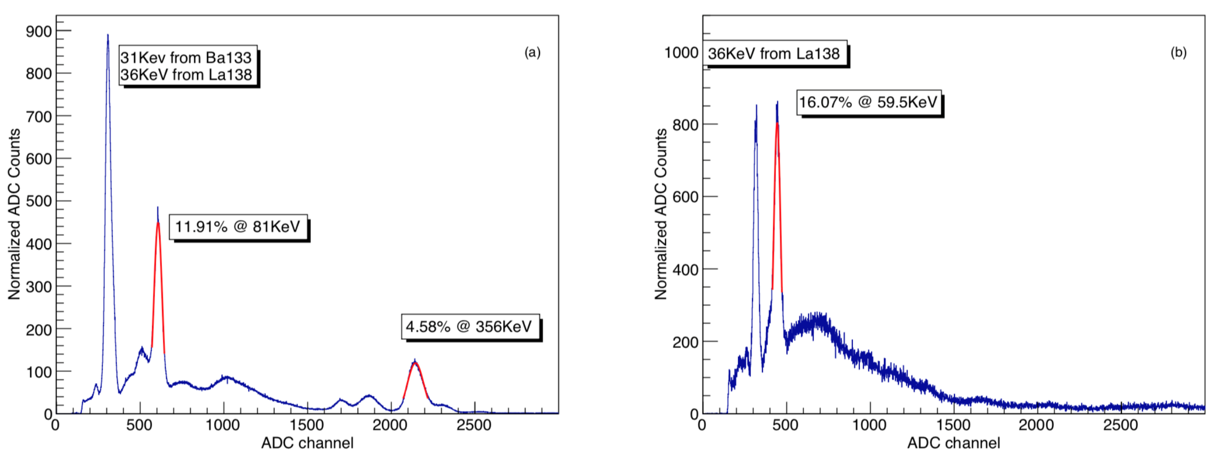

Fig. 20 Spectrum performance: (a) Barium-133 radioactive source, (b) Americium-241 radioactive source.

supply board are cold backups, and every two of them constitute a power supply channel. Each channel is responsible for supplying high voltage power to up to 13 PMTs. Using high precision digital-to-analog converter (DAC), voltage can be adjusted with a step of several hundred mV from 780∼1000 V, which meets the requirement of gain adjustment for a PMT. When the spacecraft enters the radiation belt, the high voltage power supplies should be turned down to avoid damage to PMTs due to high charge particle flux.

Table 3 Vibration Test Condition

Frequency	Test value / ($g^2 \cdot Hz^{-1}$)
20∼100	+3db/oct.
100∼600	∼0.006
600∼2000	–9db/oct.
overall	1.0g/2.25g rms
direction	X/Y/Z
time	1 min per direction

3.4 Environment Qualification and Performance Test

Some tests have been performed on the engineering prototype. In addition to verifying the performance of the detector unit, several vibrational and thermal environment qualifications were also carried out on HXI-C to evaluate whether its structural strength and assembly stability meet the assembly precision requirements. Here are some preliminary results of these tests.

3.4.1 Vibration test

Last December, the HXI prototype participated in the satellite system vibration test. Test data can match the given vibration conditions well. Measurements of the acceleration of the centroid and the top plate indicate very positive results that acceleration response enlarges less than two times. Furthermore, the first-order fundamental frequency is over 100 Hz which means that it does not couple with the satellite.

In March 2019, a vibration test of HXI-C itself was carried out. Due to the fact that strength of the transition plate is not high enough, the test condition listed below is lower than that provided by the satellite. Sine sweeps before and after vibration as well as the electrical test demonstrate that the mechanical design is rigid enough to guarantee the grids and the framework with very little deformation. The first-order fundamental frequency deduced from the sine sweep results is about 120 Hz which could fulfill the requirement proposed by the satellite and may greatly prevent HXI-C from resonance with the platform.

3.4.2 Thermal balance test (satellite system)

During the test, the design of active thermal control is verified. Temperature measuring point (20 thermistors with thermocouple) distribution described hereafter refers to the finite element model (FEM) results and total monitoring channels of the test. The thermal balance test lasted around 10 d in the thermal vacuum chamber. We choose the typically worst hot and cold cases to compare with FEM results.

The worst hot case for ASO-S occurs with an 87° orbital inclination angle aiming at the Sun. HXI-C comes through such a hot case. Test data show that the maximum temperature difference between the front and rear plates is about 0.7° C and the framework structure temperature difference is less than 1° C at the same time.

The worst cold case for ASO-S happens with a 58° orbital inclination angle aiming at the Sun. Test data indicate that temperature difference between the front and rear plates is about 0.5° C and the framework structure temperature difference is less than 1° C at the same time. The results of this test favorably match the FEM analysis results. Meanwhile, temperature difference is less than 1° C as expected on the whole. Thus, the thermal design could satisfy the demands of the thermal control.

3.4.3 Thermal cycle test

The first thermal cycle test was performed in February with the temperature range from 0° C to 40° C. However, the deformation of the HXI-C measured by SAS and a laser tracker was much larger than expected, and also exceeded the requirement. To solve the problem, several ways have been tried at the same time, such as optimizing the deformation monitoring function of SAS and improving the thermal condition.

In March, the thermal cycle test was carried out again with temperature range 22±5° C and 22±10° C (According to the results of the satellite thermal balance test, the normal working temperature of HXI-C in orbit could be 22±2° C, which is better than the designed value, 22±5° C). Test results were positive and the deformation reduced greatly compared to the pre-test. From the data provided by SAS, relative deformation and distortion were less than 10 μm and 10 arcsec respectively.

3.4.4 Performance test of HXI-S

For ensuring the reliability of observation results in orbit, the on-ground energy linearity calibration is absolutely necessary. This test has been carried out in the Hard X-ray Calibration Facility (HXCF), an adjustable X-ray beam with a double crystal monochromator, designed for the Chinese Hard X-ray Modulation Telescope satellite by the Division of Ionizing Radiation Metrology, National Institute of Metrology (Zhou et al. 2014). This facility could generate X-ray photons covering the energy range 15 keV ∼ 100 keV with monochromaticity better than 0.1%. As depicted in Figure 18, the $LaBr_3$ detectors will be placed in the test platform with a calibrated High Purity Ge detector. For energy range larger than 150 keV, an embedded Barium-133 source is used to provide several characteristic lines from 276 keV to 383 keV. The test result is illustrated in Figure 19, which shows the nonlinearity of $LaBr_3$ with PMT from energy 31 keV to 383 keV is better than 2%.

Table 4 Relative Displacement and Distortion of the Front and Rear Base Plate

Case	Distortion / ″	Horizontal displacement / μm	Vertical displacement / μm
22±5° C	0.79645	0.083	5.602
22±10° C	2.39335	–5.6997	–12.6285

The energy resolution of the whole system has been tested with the calibration source of Barium-133 and Americium-241. As visible in Figure 20, the average full width at half maximum (FWHM) resolution of the spectrometer system is about 16.07% @ 59.5 keV, 11.91% @ 81 keV and 4.58% @ 356 keV. The spectrum peak at around 300 channels of ADC derives from a combination of 31 keV CsKα X-ray in the decay of Barium-133, and 32 keV BaKα X-ray with $\sim$4 keV Auger electrons in the decay of Lanthanum-138 inside the crystal. Although the multi-source peak makes it not applicable for measuring the energy resolution @ 30 keV directly, a rough calculation based on results from radioactive sources demonstrates the energy resolution @ 30 keV is better than 22%, which meets the specifications of HXI.

4 SUMMARY

After the Phase A and Phase B development, we have completed the basic design and engineering prototype production, and identified some key technologies. Obviously, it is a challenging and tough mission for us because of its high requirement for system design and some processing technologies, such as grid production, assembly and so on. Fortunately, the measurement and test results have verified the feasibility and reliability of our design in some aspects.

The qualification model has been designed and developed since entering Phase C. At the same time, more tests are still being carried out on the engineering prototype to ensure the design and identify areas for improvement.

Acknowledgements We would like to thank Dr. Gordon J. Hurford for his great help and valuable suggestions. Drs. Säm Krucker and Alexander Warmuth are acknowledged for their helpful discussions. This work is supported by the Strategic Priority Research Program on Space Science, Chinese Academy of Sciences (Grant No. XDA15320104) and by the National Natural Science Foundation of China (Grant Nos. 11427803, 11622327, 11703079, 11803093 and 11820101002).

References

Benz, A. O. 2017, Living Reviews in Solar Physics, 14, 2
Chen, D. Y., Zhang, Z., Hu, Y. M., et al. 2019, Society of Photo-Optical Instrumentation Engineers (SPIE) Conference Series, submitted
Dennis, B. R., & Pernak, R. L. 2009, ApJ, 698, 2131
Fletcher, L., Dennis, B. R., Hudson, H. S., et al. 2011, Space Sci. Rev., 159, 19
Gan, W. Q., Zhu, C., Deng, Y. Y., et al. 2019, RAA (Research in Astronomy and Astrophysics), 19, 156
Kosugi, T., Makishima, K., Murakami, T., et al. 1991, Sol. Phys., 136, 17
Krucker, S., Hurford, G. J., Su, Y., & Gan, W. Q. 2019, RAA (Research in Astronomy and Astrophysics), 19, 167
Krucker, S., Bednarzik, M., Grimm, O., et al. 2016, Nuclear Instruments and Methods in Physics Research A, 824, 626
Lin, R. P., Dennis, B. R., Hurford, G. J., et al. 2002, Sol. Phys., 210, 3
Meier, D., Ackermann, J., Olsen, A., & Gan, W. Q. 2016, Proceedings of the ESA AMICSA & DSP, 6th International Workshop
Priest, E. R., & Forbes, T. G. 2002, A&A Rev., 10, 313
Sato, J., Kosugi, T., & Makishima, K. 1999, PASJ, 51, 127
Su, Y., Liu, W., Li, Y. P., et al. 2019, RAA (Research in Astronomy and Astrophysics), 19, 163
Warmuth, A., & Mann, G. 2013, A&A, 552, A86
Zhang, Y., Guo, J. H., Zhang, Z., et al. 2019, Nucl. Sci. Tech., 30, 128, `https://link.springer.com/article/10.1007/s41365-019-0642-y`
Zhou, X., Li, X., Xie, Y., et al. 2014, Experimental Astronomy, 38, 433